Fernández Díaz, R.; Calero-Alcarria, MDS.; Reviakine, I.; García, JV.; Rocha-Gaso, MI.; Arnau Vives, A.; Jiménez Jiménez, Y. (2021). High Fundamental Frequency (HFF) Monolithic Resonator Arrays for Biosensing Applications:
Design, Simulations, Experimental, Characterization. IEEE Sensors Journal. 21(1):284-295. https://doi.org/10.1109/JSEN.2020.3015011

High Fundamental Frequency (HFF) Monolithic Resonator Arrays for Biosensing Applications: Design, Simulations, Experimental Characterization

Román Fernández[1,2], María Calero[1], Ilya Reviakine[2,3], José Vicente García[2], María Isabel Rocha-Gaso[2], Antonio Arnau[1] and Yolanda Jiménez[1]

[1] Centro de Investigación e Innovación en Bioingeniería, Universitat Politècnica de València, 46022 Valencia, Spain
[2] Advanced Wave Sensors S.L. 46988, Paterna, Valencia, Spain
[3] Department of Bioengineering, University of Washington, Seattle, WA, 98150, USA

Abstract—Miniaturized, high-throughput, cost-effective sensing devices are needed to advance lab-on-a-chip technologies for healthcare, security, environmental monitoring, food safety, and research application. Quartz crystal microbalance with dissipation (QCMD) is a promising technology for the design of such sensing devices, but its applications have been limited, until now, by low throughput and significant costs. In this work, we present the design and characterization of 24-element monolithic QCMD arrays for high-throughput and low-volume sensing applications in liquid. Physical properties such as geometry and roughness, and electrical properties such as resonance frequency, quality factor, spurious mode suppression, and interactions between array elements (crosstalk), are investigated in detail. In particular, we show that the scattering parameter, S_{21}, commonly measured experimentally to investigate crosstalk, contains contributions from the parasitic grounding effects associated with the acquisition circuitry. Finite element method simulations do not take grounding effects into account explicitly. However, these effects can be effectively modelled with appropriate equivalent circuit models, providing clear physical interpretation of the different contributions. We show that our array design avoids unwanted interactions between elements and discuss in detail aspects of measuring these interactions that are often-overlooked.

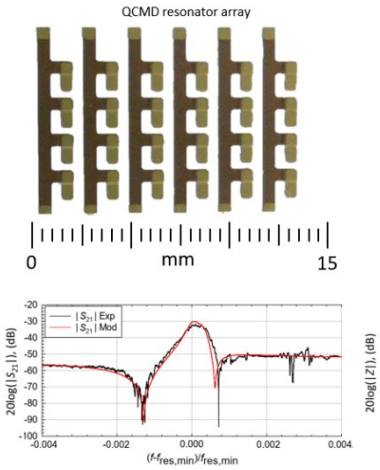

Index Terms—Biosensors, crosstalk, finite element modeling simulation, food safety, monolithic arrays, nanotechnology, pathogen detection, piezoelectricity, point-of-care, QCMD, quartz crystal microbalance, quartz resonators

I. Introduction

A wide range of bioanalytical applications requires robust and compact detectors (sensors) for rapid and reliable quantification of multiple analytes in small sample volume

lab-on-a-chip (LoC) devices. Applications range from Point-of-Care (PoC) devices for disease diagnostics, health monitoring, and treatment monitoring in personalized medicine[1], [2] to devices for analysis of active substances and pathogens in food and environmental safety [3]. It is foreseen that LoC devices will replace costly conventional analytical methods that require trained personnel, centralized laboratories, relatively large sample volumes, and complex sample preparation protocols.

Critical requirements for the design of the sensors for LoC devices include simplicity and low cost, high sensitivity and specificity, low volume, portability and high-throughput. These sensors should be able to reliably detect specific analytes present at very low concentrations against a strong non-specific background [4]; allow deployment "in the field" (non-centralized laboratories, food processing plants, supermarkets, hospitals, patients' homes); have low sample/reagent consumption; and enable simultaneous monitoring of multiple analytes at high speed to improve throughput [1], [2], [5]–[7]. Quartz Crystal Microbalance with Dissipation (QCMD) [8], [9] technology is emerging as a feasible candidate for their design, because it has the capability to satisfy all of those requirements.

QCMD is a sensing technique based on piezoelectric resonators, typically a quartz plate that is electrically excited to oscillate in a thickness-shear mode at its resonance frequency. Interactions between the resonator and its environment are sensed as changes in its resonance frequency and bandwidth (dissipation) [8], [10], [11]. In its simplest form, QCMD senses mass of the material absorbed at the resonator surface[12]. Specificity is conferred by modifying resonator surfaces with antibodies or antigens for performing direct-, sandwich-, or competitive immunoassays [13], while surface modification with DNA probes allows for DNA-based detection; this works even in complex samples without further purification [14]. The sensitivity of QCMD-based immunoassays is, in the clinically relevant range, comparable to that of ELISA [13], and be further improved using the so-called high fundamental frequency (HFF) resonators [15], [16], with frequencies in the 50 MHz – 150 MHz range [17]–[19]. HFF resonators offer an improvement in sensitivity because the frequency shift due to a given load scales with the square of the resonance frequency according to Sauerbrey relationship [12]. In practice, the improvement has so far been more modest than predicted by theory [20], but HFF resonators offer a unique approach to miniaturizing and parallelizing QCMD-based assays through the design of the monolithic resonator arrays with low-volume elements, thus also improving the throughput and reducing reagent consumption. Design and testing of such monolithic HFF QCMD resonators arrays are the focus of the current contribution.

Our array design is shown in Fig.1. Arrays consist of 6 columns of 4 resonator elements each. The design of each of the array elements is based on that of the individual 150 MHz HFF resonators we reported previously [21]: Individual resonators had a one-sided inverted MESA geometry and were optimized in terms of size, electrode geometry, and inverted MESA region thickness for spurious mode suppression, operation in liquids, as well as constraints imposed by the manufacturing and integration with fluidics and electronics [18], [19], [22]. Here, we characterize physical and electrical properties of these arrays (surface topography and roughness; resonance and inharmonic responses; interactions between array elements), and include a preliminary testing operation of the arrays in liquid.

Monolithic QCMD arrays designs have been presented previously. The initial focus was on gas sensing applications [23]–[25]. Sensing applications in liquids started

appearing more recently [24]–[32]. These designs demonstrated the potential of monolithic sensor arrays for improving the throughput of the detection of biological samples in liquid environments with QCMD, but they also illustrated some of the problems associated with their design and implementation. In particular, the field of HFF resonator arrays remains in its infancy, and much remains to be done in terms of optimizing their design for practical applications. In this work, we investigate interactions (interference, crosstalk) between array elements, and how these interactions are measured and modelled. We compare experimental measurements of the crosstalk between array elements with the results of the finite element method (FEM) simulations. Our analysis reveals that the FEM simulations do not reproduce experimental results unless the parasitic grounding phenomena arising from the interface to the readout systems are explicitly taken into account; these have not previously received attention in the literature. We propose a lumped element equivalent circuit model that is much simpler than the FEM simulations. This simple model is able to provide a reliable representation of the experimental measurements. Moreover, it also allows a direct identification of the physical contributions to the experimentally measured crosstalk between the array elements. This has practical implications for the design of monolithic HFF QCMD arrays because it allows a quick estimation of the inter-element interference and a means to identify its causes.

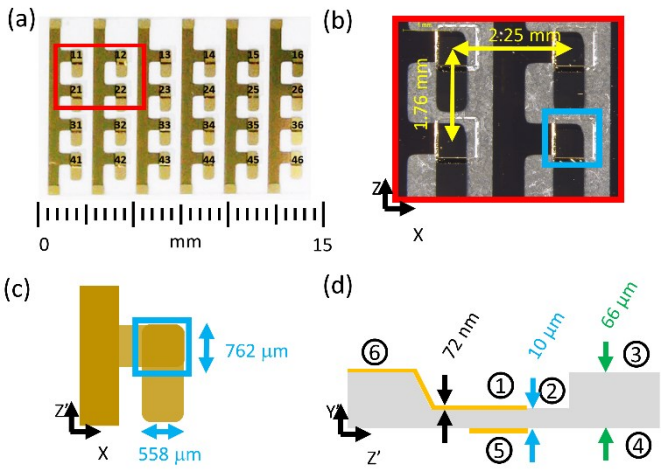

Fig. 1. The main result of this work is the 24-element monolithic QCMD resonator array. A photograph is shown in (a). Numbers indicate the row and the column of each element. (b) An optical micrograph of four of the array elements (outlined with a red box in (a)). The image is taken in transmission, and therefore, the gold appears black, while quartz appears light-grey. Center-to-center distances between the individual array elements along the X and the Z' directions are indicated. (c) and (d): top view and side view of the individual array elements, respectively. The dimensions of the square MESA region, 762 µm × 762 µm, and the width of the gold electrode, 558 µm, are indicated in (c), while thicknesses of the substrate region, the MESA region, and the electrodes (gold with a Cr adhesion layer), are indicated in (d). Quartz crystallographic axes indicated in (b) also apply to (a). Note, that the working surface of the array is the one with the common electrodes, which in this figure is facing down. The "back" surface is the one with the MESA region.

II. Materials and Methods

A. Materials

Nanopure water used in this study was either analytical grade water (Panreac Química SLU, Barcelona, Spain), or produced with a Smart2Pure UVUF water purification system (Thermo Fisher Scientific, Barcelona, Spain). Distilled water was purchased at the local supermarket. 99.5% pure ethanol was from Panreac Química SLU. Ultra-pure nitrogen was from Al Air Liquide España, S.A. (Valencia, Spain), distributed with a gas filter pistol equipped with a 1 µm pore diameter PTFE filter (Skan AG, Allschwil, Switzerland). Acetone was of technical grade (Panreac Química SLU).

B. Array Manufacturing

Resonator arrays based on the one-sided inverted MESA technology were manufactured from 66 µm thick AT-cut quartz wafers using photolithographic, wet etching, and thermal evaporation/filament plating technologies [18]. A photo of one of such arrays is shown in Fig.1, where the dimensions are also indicated. These arrays are designated AWS-Array2-24-150.0M (Advanced Wave Sensors S. L., Valencia, Spain) for future reference.

C. Array Preparation, Cleaning

Prior to use, the arrays were treated for 10 min in UV/ozone cleaner (BioForce Nanosciences Inc., Chicago, IL, USA), rinsed with ethanol, distilled water, dried with a stream of filtered nitrogen, and again treated with UV/ozone for another 10 min.

D. Array Characterization

1. Physical Characterization

The arrays were examined optically with an MZ APO Stereomicroscope from Leica Microsystems (Leica Microsistemas S.L.U, Barcelona, Spain). Surface morphology, topography & roughness, as well as presence of contamination, electrode alignment and presence of the etching channels in the quartz, were investigated with atomic force microscopy (AFM), scanning electron microscopy (SEM) and optical profilometry (OP).

SEM was performed with a Field Emission Scanning Electron Microscope (Ultra 55 FEGSEM, Zeiss, Oberkochen, Germany) at a working distance of 3.8 mm with an accelerating voltage of 2 kV and a vacuum level of 8×10^{-7} mbar at the chamber. The sample was mounted using a colloidal silver adhesive (SPI Supplies, West Chester, PA, USA).

AFM was performed with a Multimode 8 Atomic Force Microscope (Bruker, Billerica, MA, USA) equipped with a JV vertical engage scanner and a silicon tip with a spring constant of 26 N/m and a resonance frequency of 300 kHz (OTESTA-R3, Bruker, Billerica, MA, USA). For imaging, the arrays were attached to metal pucks with double-sided tape and imaged in tapping mode at scanning rates of 0.5 Hz^{-1} (depending on the scan size) at optimal gain. Images were acquired in air. To acquire some of the images, arrays had to be cut.

The profile of the MESA surface of the array was analyzed with a Surftest SJ-410 profilometer (Mitutoyo, Kanagawa, Japan) with a 2 µm radius and 60º angle 12AAC731 tip. The surface was scanned with a rate of 0.5 mm/s.

2. Electrical Characterization

Complex admittance spectra of the array elements, as well as the scattering parameter S_{21} used to evaluate crosstalk between array elements, were measured with a DG8SAQ VNWA 3 Vector Network Analyzer (SDR-Kits, Melksham, Wiltshire, UK).

In order to connect the arrays to the network analyzer, we adapted a benchtop robot (F4300N.1, Fisnar Inc., Germantown, Wisconsin, USA, Fig. 4a) to house two custom-

designed printed circuit boards (PCBs): one mounted on the base of the robot, and the other one on its moving arm (Fig. 4b, c). The array studied was effectively sandwiched between the two PCBs, mounted with the MESA region facing up. In this configuration, an electrical contact is established between the common electrode of the array (bottom in Fig. 1a) and the bottom PCB, which is grounded, on one hand, and the individual electrodes of the different array elements and the top PCB through 0.6 mm diameter spring contacts (Peak Test, Chester-Le-Street, County Durham, UK), on the other hand. The top PCB has five spring contacts, four of which are connected to four array elements, while the fifth one connects the bottom PCB to ground. The spring contacts assure an electrical connection without generating an uncontrolled pressure that could break the array. With this setup, we measured the admittance of each of the array elements, and cross-talk between pairs of elements (S_{ij}, $S_{i+1,j}$); (S_{ij},$S_{i,j+1}$); (S_{ij},$S_{i+1,j+1}$) with i = 1··6 and j = 1··4 along the X direction, Z' direction, and the diagonal. The setup was calibrated by placing the calibration components at the PCB level. The surfaces of the PCBs were degreased with acetone immediately prior to measurements.

Complex admittance spectra were used to visualize spurious modes and quantify the separation between the fundamental and the first spurious mode for each of the array elements. Around the resonance frequency, the complex admittance spectra were fit to a phase-shifted Lorentzian model proposed by Petri and co-workers [33], to obtain maximum conductance, G_{max}; resonance frequencies, f_{res}; and bandwidths, Γ, of the array elements. Quality factors, Q, were calculated from f_{res} and Γ as $Q=f_{res}/(2\,\Gamma)$. The phase-shifted Lorentzian provides a robust fit to the data that is relatively insensitive to the residual calibration imperfections.

Measurements of the S_{21} parameter for characterizing the cross-talk between the elements were performed by exciting one array element with an incident power of 1 mW (0 dBm) and recording the power at the neighboring array element, on each of the array element pairs for the three directions (X, Z', diagonal).

E. Modelling and Simulations

1. Equivalent Circuit Model

An equivalent circuit model was developed to analyze the cross-talk between array elements based on the monolithic crystal filter topology (MCF, Fig.10a) [34], [35].

The equivalent circuit consists of two resonators. Each resonator is represented by a Butterworth-van Dyke (BvD) circuit containing the standard resistor R_i, inductor L_i, and a capacitor C_i connected in series representing the motional, or acoustic, branch, and a capacitor C_{0i}, connected in parallel, representing the electrical branch that describes the static and parasitic capacitances; i = 1 or 2 is one of the two coupled resonators. The two resonators shared a common electrode, grounded via parasitic elements consisting of an inductor L_p and a resistor R_p as shown in Fig.10 b.

The coupling between the two resonators is represented by a parallel network of a resistor R_e and a capacitor C_e, and an inductor L_a. R_e and C_e, represent electrical coupling, and L_a acoustic coupling, respectively. Further details are provided in Section S3 of the Supporting Information. Such modified BvD circuit models of coupled resonators have been introduced in the literature previously [34]–[36].

2. FEM Simulations

3D FEM simulations of the coupled resonators were used to further understand crosstalk between the array elements. They were implemented in the commercial software package ANSYS version 19 (ANSYS, Canonsburg, PA, USA) running on a high-performance workstation (C50000 Pro workstation, Orbital Computers LLC, WA, USA). As a starting point for the simulations, we took the numerical model of a single 150 MHz

HFF-QCM resonator we have previously developed [21], since this individual resonator served as the basis for the design of the array elements.

Material properties were assigned based on the 'SOLID226' coupled-field element of the ANSYS libraries that captures the coupling between displacements and electrical potentials in piezoelectric materials. Values for the physical properties of AT-cut quartz used in the calculations are listed elsewhere [21], [37], [38]. To model the detuning, the density of the quartz was slightly modified for one of the resonators. The damping factor was set to 5×10^{-5}. The structure was meshed according to the procedure described in ref. [21], which also describes the electrode effects. The mesh is also shown in Fig. 9a and 9b. More details about FEM modelling can be found in Section S2 of the Supporting Information.

III. Results and Discussion

A. The Geometry of the Monolithic HFF-QCMD Arrays

The key result of this work is the 24-element array design shown in the optical micrographs in Fig 1a, b. The elements are organized into 6 columns of 4 elements each. The columns are defined by the six long electrodes running the size of the array in the Z' direction, with four short rectangular finger-like electrodes extending away from each column along the X direction. The column electrodes are grounded, thus effectively forming one electrode common to all 24 array elements. This common electrode constitutes the "working" side of the array. It faces the sample.

On the other side of the array, the short rectangular electrodes are oriented with their long axes along the Z' direction and are connected to the driving circuitry individually. Array elements (numbered with a row and a column index in Fig. 1a) consist of square one-sided inverted MESA structures (visible in Fig. 1b) sandwiched between the two sets of the short rectangular electrodes that are oriented orthogonally to each other. One such individual element is depicted schematically in Fig. 1c. Element design is based on the individual 150 MHz HFF resonators we reported previously [21].

The side view of the MESA region, with dimensions, is shown in Fig. 1d, where various numbers refer to the different zones of the array element surfaces. In particular, zones 1 and 6 correspond to the surface of the rectangular electrode on the etched side of the array, while zone 5 corresponds to the surface of the rectangular electrode on the flat side of the array (grounded, working surface). Zones 2 and 3 refer to the bare quartz on the etched side of the array, and zone 4 on the flat side. The flat side of the MESA corresponds to the working side of the array.

B. Physical Characterization of the Arrays

The arrays were fabricated by a combination of photolithography and wet etching processes. These methods have previously been used by us [21] and others [18], [24], [39]–[41] to successfully fabricate high-quality HFF-QCMD resonators and monolithic resonator arrays based on the inverted MESA geometry. The process is cost-effective, robust, and yields low-roughness resonator surfaces, but it can result in etch channels and etch pits that are detrimental to the resonator performance [41]–[44]. We investigated the morphology and roughness of the resonator surfaces and reproducibility of the individual features across the array elements by optical microscopy, FEGSEM, profilometry, and AFM. The results are presented in Table I, Fig. 2 and Fig. 3.

A FEGSEM image of a typical array element is shown in Fig. 2a. The square inverted MESA region is readily visible, and the rectangular gold electrode extending from the surrounding buffer to the MESA region itself (zones 1 and 6) can be identified. Note, that the inverted MESA is bound by the edges with different slopes due to the anisotropy of the etching process [43]–[45]. The electrode is seen to closely follow the slanted edge of

the inverted MESA (on the left in Fig. 2a), insuring proper conductivity across the electrode [44]. The two electrodes are perpendicular to each other. This makes our design robust to mask misalignments.

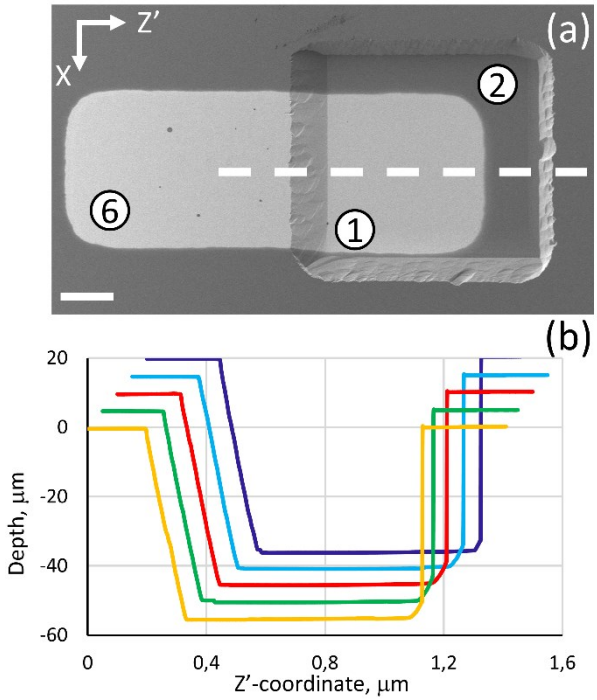

Fig. 2. Physical Characterization of the Arrays (a) A FEGSEM image of one of the array elements showing the inverted-MESA region (zone 2) and the gold electrode (zones 1 and 6). Zone numbers refer to Fig. 1d. White dashed line indicates where the surface profiles, shown in (b), were taken. Axes indicate the crystallographic orientation of the AT-cut quartz. Scale bar is 200 µm. (b) Surface profiles measured with a profilometer along the direction indicated with the dashed white line in (a). Profiles are offset by 0.05 µm along the abscissa and by 5 µm along the ordinate relative to each other. Note the characteristic difference in slopes between the two sides of the inverted MESA region that arises from the anisotropy of the etching process.

The reproducibility of the depth and size of the inverted MESA region can be evaluated from the profilometry traces shown in Fig. 2b. Here, each color represents a different array element from two different arrays. The fabrication process was extremely reproducible, with the etching depth of 55.9 µm ± 0.5 µm, which is convenient for reliable operation in automated data acquisition systems.

TABLE I
VALUES OF ROUGHNESS

Zone (see Fig. 1d)	R_a (nm) 2.5 µm x 2.5 µm
1 (Gold, etched, MESA)	0.67 ± 0.01
2 (Quartz, etched, MESA)	0.72 ± 0.06
3 (Quartz, etched, buffer)	0.9 ± 0.1

4 (Quartz, flat, buffer)	0.34 ± 0.04
5 (Gold, flat, MESA)	0.79 ± 0.2
6 (Gold, etched, buffer)	1.02 ± 0.08

Calculated from the AFM images of the different regions (zones) of the resonator elements of an array, such as those shown in Fig. 3. Zone numbers are specified in Fig. 1d. "Etched" and "flat" refer to two sides of the array.

FEGSEM images reflect the uniformity of the surface finish of the array elements after the etching process. This is further investigated on a smaller length scale in Fig. 3, where the AFM images of zones 1, 2, 4, and 5 of one of the array elements are shown. Apart from a few spikes caused, most likely, by contamination of the samples during the cutting and mounting of the array on the stage of the AFM, the images appear devoid of any large-scale features. This is consistent with the SEM results presented above. The values of the roughness calculated from these images for the different zones are summarized in Table I. In all of the zones, the roughness is ~ 1 nm or less, (Table I). Note, that on the flat side, the gold deposition increases the roughness (c.f. zones 4 and 5 in Table I), while on the etched side, it decreases the roughness (c.f. zones 1 and 2 in Table I). This arises from the finite size of the gold grains, which are larger than the features of the polished quartz face but smaller than the features of the etched quartz face.

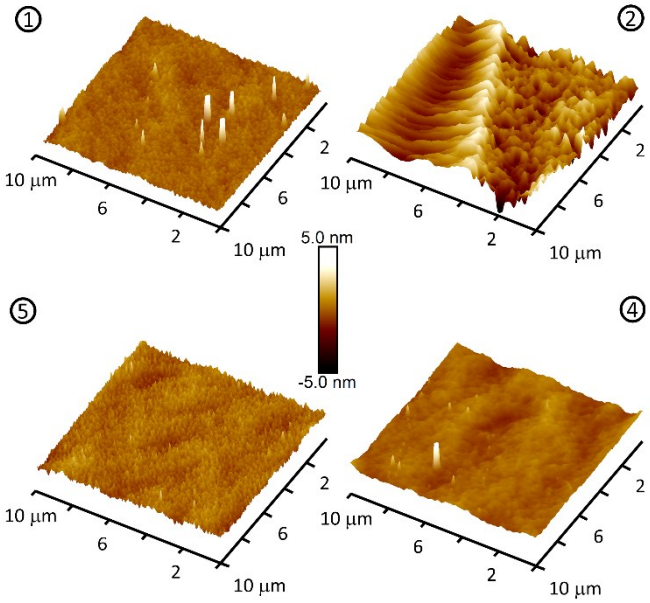

Fig. 3. High-resolution Surface Characterization of the Array Elements AFM images of the different regions of one element of an array. Encircled numbers refer to the zones defined in Fig. 1d: 1) Surface of the gold electrode in the MESA region, 2) MESA region without the electrode, 4) Bottom surface of the resonator without the electrode and 5) Surface of the gold electrode on the bottom face. A few white regions (spikes) are seen in the images of zone 1 and zone 4.

The roughness of the resonator surfaces is important for acoustic sensor performance in liquids: gas bubbles can be trapped in the roughness during the wetting of the sensors; new energy dissipations channels arise from the hydrodynamic effects at the oscillating sensor surface; finally, roughness affects adsorption behavior of biomolecules. These effects are minimized in our case by etching the blanks from one side only. This leaves the working side of the array polished and untouched, exhibiting sub-nm roughness

(Table I) that is, in fact, better than that of the state-of-the-art resonators (~ 1 nm [46]). These values are of the same order as those reported in the literature (see Table II). Indeed, the only currently available method of improving the surface roughness of the resonators beyond this range is through the ultra-flat technology that has not yet been generalized to the HFF resonators [46], [47].

In summary, the physical characterization of the arrays revealed array elements with highly reproducible lateral dimensions and depths, devoid of large-scale surface features that would impede their operation, with surfaces roughness of the order of ~ 1 nm.

TABLE II
COMPARISON OF QUALITY FACTOR Q AND ROUGHNESS RA REPORTED BY DIFFERENT MANUFACTURING TECHNIQUES

Reference	Frequency (MHz)	Ra (nm)	Q (in air)	Fabrication process
Values in this work	150	1	12000	Wet etching
Abe et al. [48]	94	2	30000	Deep RIE
Liang et al. [40]	84	--	25000	Wet etching
Hung et al. [49]	83	4-8	12000	Deep RIE
Liang et al. [40]	73	--	24000	Wet etching
Kao et al. [25], [27]	60-70	2	22100	Deep RIE
Liang et al. [40]	60	--	27000	Wet etching
Buettgenbach et al. [44]	48	10	50000	Wet etching
Liang et al. [40]	47	--	25000	Wet etching
Zhang et al. [50]	45	--	13200	Wet etching
Zimmermann et al. [18]	30	--	37.000	Wet etching
Abe et al. [51]	20	2	2000	Deep RIE

RIE: Reactive Ion Etching

C. Electrical Characterization of the arrays

1. Resonance parameters

To characterize resonance behavior of the array elements, their complex admittance spectra were measured using a vector network analyzer. To this end, the arrays were mounted in a home-made device adapted from a bench-top robot shown in Fig. 4. Resonance frequencies and quality factors are shown in Fig. 5 and Fig. 6, respectively. The data reveal compact distributions of frequencies and quality factors from 26 different arrays, with averages of 149 MHz± 0.2 MHz and $(1.2 \pm 0.1)\times10^4$ for the resonance frequency and quality factor, respectively (measured in air).

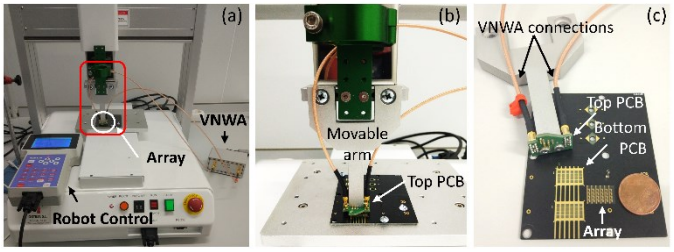

Fig. 4. Home-made robotic setup for the electrical characterization of the arrays. (a) Overview of the base with the movable arm and the network analyzer (VNWA). Location of the array, under the movable arm, is indicated with a white circle, while the red outline defines the region shown in (b). (b) Enlarged view of the movable arm, with the top PCB, and VNWA connection cables visible. In this configuration, the array is not visible as it is sandwiched between the two PCBs. They are shown in (c) in the open configuration. (c) The PCB assembly: bottom PCB with an array and a 5¢ euro coin to give the idea of the scale; Movable arm, detached from the robot, with the top PCB and the VNWA connection cables.

The variation in the values of the resonance frequency between array elements is similar to that we reported for the single sensors previously [21]. There is a slight systematic trend visible in Fig. 5 with the resonance frequencies decreasing across the columns, most likely due to uneven etching that will be fixed in the subsequent batches. The detuning between sensors caused by the manufacturing deviations, even though unintended, is beneficious for crosstalk reduction [38].

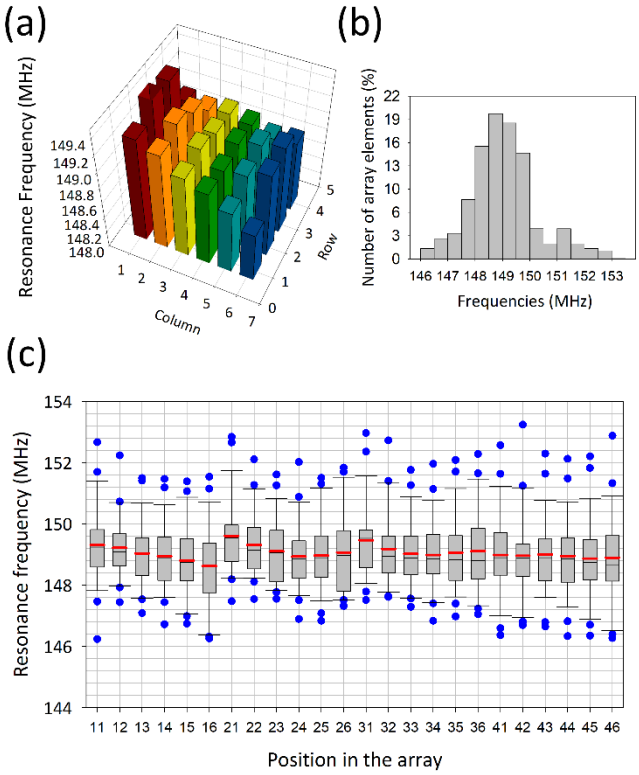

Fig. 5. Resonance Frequencies of the Array Elements The results from 26 arrays are shown. Measurements were performed in air. (a) A 3D bar plot of the average resonance frequencies of the array elements as a function of their position in the arrays. (b) A histogram of the resonance frequencies of the array elements depicting their overall distribution. (c) A box plot of the resonance frequencies of the array elements as a function of position in the array. Red lines: means; black lines: medians; the box defines

25th and 75th percentiles, while the error bars define 10th and 90th percentiles, while blue filled circles show outliers.

The observed quality factors of the array elements can also be compared with the theoretical limit estimated according to the relationship $Q \cdot f_{res}=1.6\times10^3$ Hz [20]. For the resonance frequency of 150 MHz, this relationship yields the expected value of $\sim 1.1 \times 10^5$ for the maximal attainable quality factor. The experimentally observed values are within an order of magnitude lower than of this theoretical limit. They are close to what we have previously reported for the individual 150 MHz resonators of the same design (9.5×10^3 [21]). Furthermore, we have previously obtained quality factors of $(4.4 \pm 0.4) \times 10^4$ for the 50 MHz resonators and $(2.5 \pm 1.0) \times 10^4$ for 100 MHz resonators; the measurements were performed with the same setup as shown in Figure 4. The theoretical limits for these resonators are 3.2×10^5 and 1.6×10^5, respectively. The measured values are also similar to the ones reported in the literature (see Table II). This comparison with our own and literature values for various HFF resonators reveals that the quality factors of HFF resonators are typically 1 – 2 orders of magnitude lower than expected theoretical limits. According to some authors, some surface features (such as etch pits, etching channels or large-scale roughness) or departures from parallelism tend to reduce the quality factor of the resonators [42]–[44], [52].

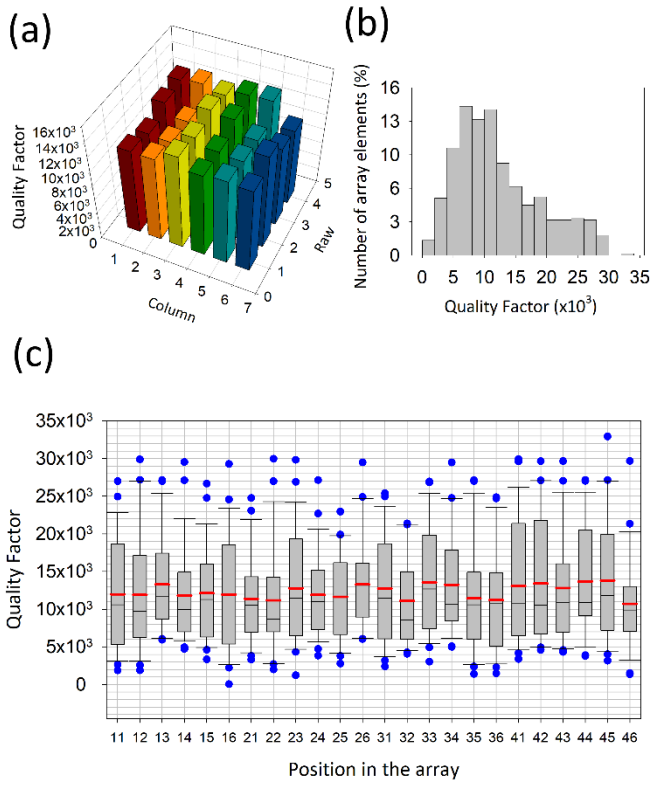

Fig. 6. Quality Factors parameters of the Array Elements. Results from 26 arrays are shown. (a), (b), and (c) are the same as in Fig. 5, but for the quality factor.

2. *Analysis of Inharmonic Sidebands*

Spurious modes may be an issue for sensing applications because coupling between them and the harmonic mode takes energy from the latter [18], [22]. This effect is more dramatic in liquid-media applications [18], [53] and the problem is more acute with the HFF resonators because for higher fundamental frequencies, inharmonics are relatively closer to the harmonic mode than in the case of lower fundamental frequencies [22].

Suppression of inharmonic modes is achieved by optimizing electrode geometry (electrode surface area and thickness) relative to the geometry of the inverted-MESA region based on the energy trapping principle developed for the classical QCMD resonators. The so-called plate-back equation is used to estimate the necessary electrode thickness [22], [54], and a compromise is then found between spurious mode suppression, conductivity, and the resonator quality factor [21], [27], [38], [55]. We have optimized electrode geometry for the individual 150 MHz resonators, as described in our previous work [21]. Here, we study the effect of their integration into the array on the inharmonic behavior by comparing experimentally measured conductance of the array elements as a function of frequency (Fig. 7a, b) with the results of the FEM simulations of the individual resonators (Fig. 7c). Heatmaps of conductance as a function of frequency show the detuning between the array elements (Fig. 7a). For an easier quantification of inharmonic separation, the same heatmaps are shown in Fig. 7b as a function of normalized frequency, f/f_{res}, where f_{res} is the resonance frequency of each array element.

For most of the array elements, the intense fundamental mode <111> appears at $f/f_{res} = 1$, followed by the inharmonic modes at higher frequencies. Significantly, the harmonic analysis performed by FEM simulations of the individual resonators accurately predicts the localization of the inharmonic modes found in the array elements experimentally (dashed lines in Fig. 7b). In particular, the odd modes <113>, <131> and <133> (black dashed lines in Fig. 7b) appear in all of the array elements as expected on theoretical grounds at frequencies that fit very well with the predictions of the FEM simulations for the individual resonators [21]. The separation between the fundamental <111> and the first of the odd inharmonic modes <113> is ~ 300 kHz or 0.003 in terms of f/f_{res}, which agrees well with the results presented by Buettgenbach et al. for a 50 MHz HFF resonator [44]. This separation is enough for measurements in aqueous media, but it should be made as wider as possible within the limits set by manufacturing restrictions.

The main difference between the predictions of the FEM simulations for the individual resonators and experimental results obtained with the arrays is that even modes (<112>,<121>,<122>,<132>,<114>,<132> and <124>) are also visible in some elements of the arrays, as a consequence of the slight asymmetries existing in the real resonators (white dashed lines in Fig. 7b) [22]. On the other hand, the misalignment during the array fabrication process, apparent in the FEGSEM images (Fig. 2a), lead to the asymmetries in the electrode configuration and different electrode thickness/effective surface areas for the different array elements, translating into differences in the spectra. These effects are minor, however. Apart from these two aspects, the modal behavior of the array elements is well-predicted by the FEM simulations of the individual resonators and is unaffected by their being part of a monolithic array.

3. Analysis of the interactions between array elements (crosstalk)

The purpose of the resonator arrays is to enable parallel measurements with each of its elements functioning independently of each other. Therefore, the extent of the interactions between the elements is an important consideration.

Experimentally, interactions between array elements are measured through the scattering parameter S_{21} shown in Fig. 8. It is immediately clear that the cross-talk between array elements in each of the three directions is, for all intents and purposes, negligible and our design is appropriate for parallel individual measurements: the experimental maximum value in $|S_{21}|$, that is ~ – 32 dB at the most with averages values of less than – 50 dB (Fig. 8a – c). These values agrees well with those reported by other authors: ~-30dB for the 3×3 66 MHz array [25], [27]; ~-50dB for the 4×4 43 MHz array [24], and < -40dB for the 2×2 10MHz array (with average values smaller than - 60dB) [56].

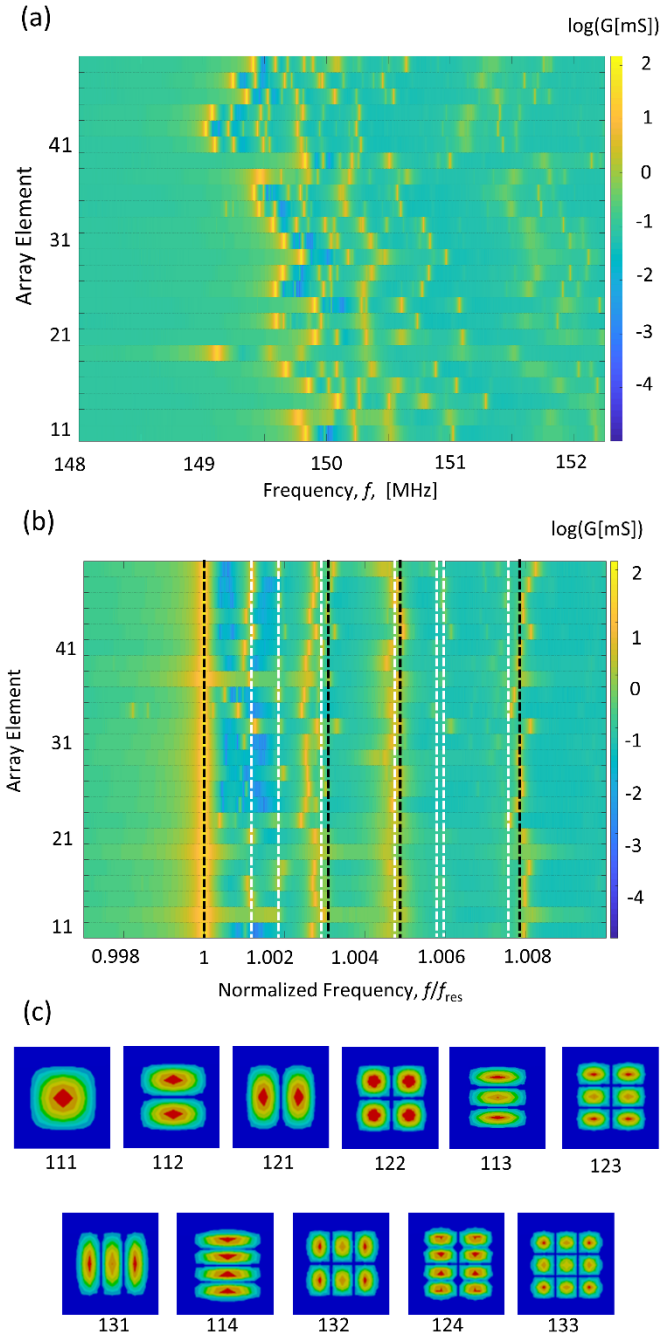

Fig. 7. Inharmonic Analysis of the Array Elements. Heatmaps of conductance as a function of frequency, f, (a), and as a function of normalized frequency, f/f_{res}, where, f_{res} is the resonance frequency of the array element, (b), for different array elements. Representative results for one array are shown. The most intense (highest conductance) mode is the fundamental, <111> mode that appears at $f/f_{res} = 1$. Dashed lines in (b) refer to the different inharmonic modes, black for odd, and white for even. The frequencies of the modes, and their displacement patterns that are shown in (c), were calculated with modal analysis simulations of individual resonators [18].

The experimental observation of negligible cross-talk is supported by the results of the FEM simulations (Fig. 9) that show lack of acoustic interactions between array elements ($|S_{21}|$ below -50dB) and lack of displacement in the passive resonator when the active neighbor is excited (see Fig. 9d).

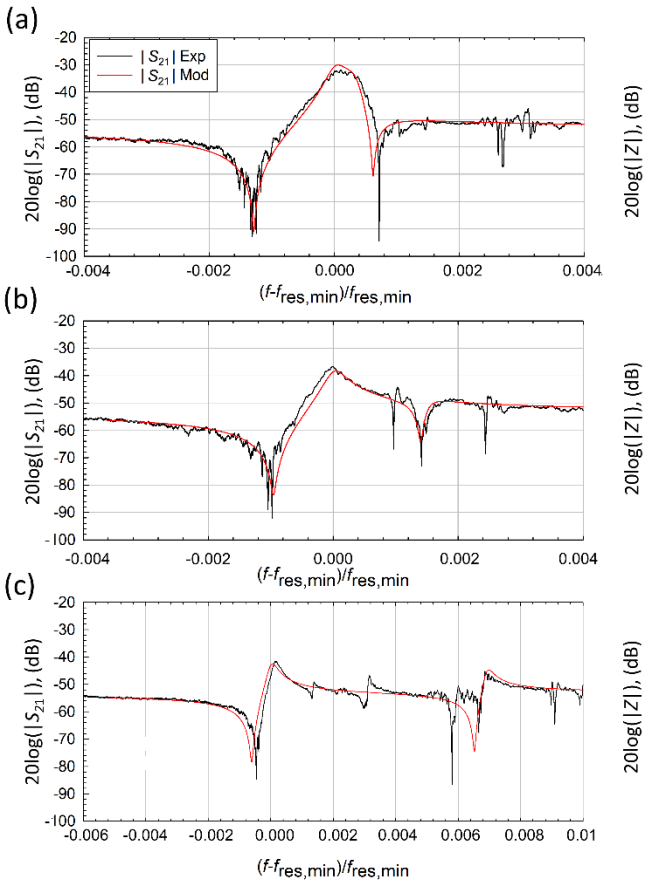

Fig. 8. Cross-talk analysis: results. Plots of the scattering parameter, $|S_{21}|$, as a function of frequency normalized to the resonance frequency of the element with the lower resonance frequency, $f_{res,min}$, for three different values of detuning $\Delta f_{ij} = f_i - f_j$, where i^{th} element is the active one and j^{th} element is the passive one. For $|S_{21}|$, the experimental results are shown in black, and equivalent circuit model calculation results—in red. Equivalent circuit model parameters were: $C_1 = C_2 = 5.73$ fF, $C_e = 32$ fF, $R_e = \infty$ Ω, $L_a = 0$ H, $C_{01} = C_{02} = 2.29$ pF, $L_p = 2$ nH and $R_p = 0$ Ω, $f_{res,\,j} = f_{res,\,i} + \Delta f_{ij}$. Furthermore, in (a), $f_{res,1} = 148.1$ MHz, $\Delta f = 49$ kHz, $R_1 = 7$ Ω, and $R_2 = 4$ Ω; in (b), $f_{res,1} = 147.5$ MHz, $\Delta f = 212$ kHz, $R_1 = 12$ Ω, $R_2 = 11.4$ Ω; in (c), $f_{res,1} = 147.3$ MHz, $\Delta f = -1009$ kHz, $R_1 = 13$ Ω, and $R_2 = 15$ Ω.

Similarly, analytical calculations based on MCF filters design also predict that acoustic coupling should be minimal. Indeed, the coupling strength K can be easily estimated from the geometry of the array and the properties of quartz according to the following expression [34]: $K = \frac{3c_{11}}{8\rho f_{res}^2 \phi_x^2} e^{-\xi d}$. Here $c_{11}=8.674\times10^{10}$ N m^2 is the elastic coefficient of AT quartz in the X direction, f_{res} is the resonance frequency of the uncoupled resonators (assumed to be the same in this case; no detuning), ρ is the density of quartz, and d is the distance between the resonators along the X direction (2.25 mm). ξ is the propagation constant for the shear-thickness mode, defined as $\xi = \frac{2.298}{t}\Delta^{1/2}$, where t is the thickness of the resonator and Δ is the so-called plate-back, $\Delta = \frac{f_s - f_{res}}{f_s}$, where f_s is the resonance frequency of the quartz plate without the electrodes. In our case, $f_s \approx 165$ MHz, $f_{res} \approx 150$ MHz, giving $\Delta \sim 0.0909$ and $\xi \sim 69287.3$. $\phi_x = d + 2r + \frac{0.418t}{\Delta^{1/2}}$ is the effective length of the vibration volume along the X axis, where r is the electrode dimension in the

X direction; in our case, this is taken for the individual electrodes on the etched side of the array, or 550 µm, giving $3 \cdot 10^{-3}$ for ϕ_x. Plugging the numbers into the expression for K, one arrives at a value of ~ 10^{-74}. In other words, in our arrays, the elements are not expected to interact acoustically.

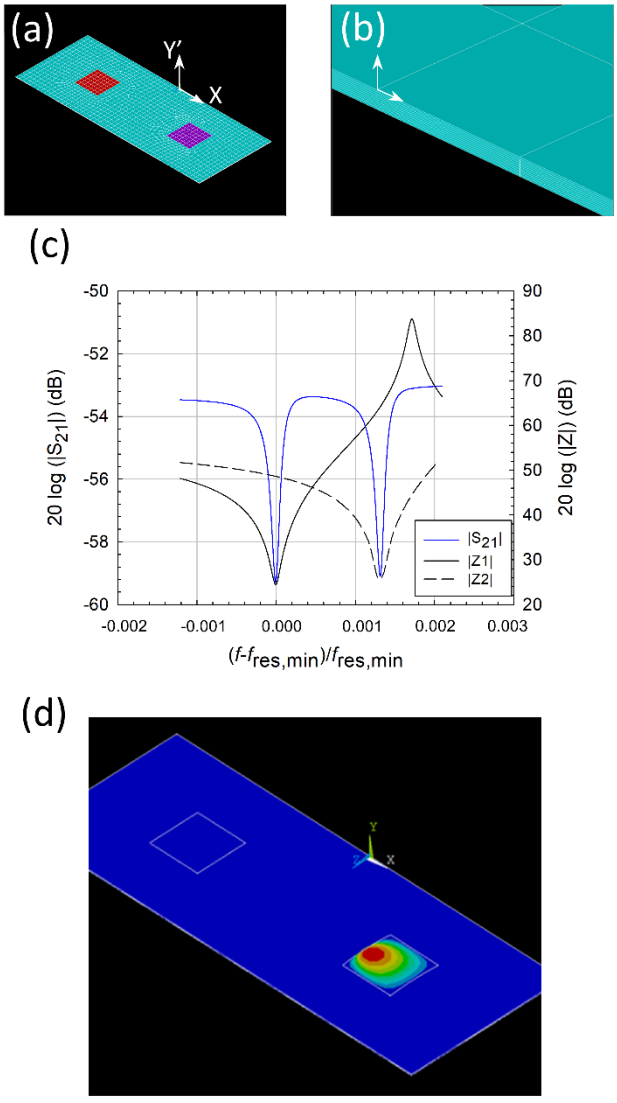

Fig. 9. Cross-talk analysis: FEM simulations. Simulation geometry and meshing. (a) Two resonators on the same AT quartz substrate are shown, with the mesh indicated. Mesh size was 50 µm × 50 µm. The distance between the two resonators was 2.25 mm (element-element distance in X direction of the manufactured array). (b) View of one of the mesh elements illustrating the meshing in the thickness direction. The substrate thickness was 10 µm, meshed into 10 slabs. Axes in (a) and (b) indicate crystallographic directions. (c) A plot of $|S_{21}|$ extracted from the simulations as a function of the normalized frequency and the corresponding impedances Z. Detuning was $\Delta f = 200$ kHz. To bring the values of $|S_{21}|$ away from resonance in the FEM simulations into register with the experimental ones, a capacitor with a value of ~ 23 fF, had to be explicitly introduced into the FEM simulations. (d) Patterns of instantaneous displacement in the active (right) and passive (left) resonators. There is no evidence of displacements in the passive resonator when the active one is excited with 0.5 V.

Interestingly, however, the FEM simulations do actually not reproduce the

experimentally observed dependence of S_{21} on frequency: the peak in S_{21} visible in Fig. 8a – c is absence in Fig. 9c. To understand this discrepancy, we constructed an equivalent circuit model based on the classical MCF topology [34], [35].The model proposed here, shown in Fig. 10b, adds new elements L_p and R_p to the well-known model used in MCF theory to account for the parasitic electrical grounding effects in the experimental setup.

The correspondence between the predictions of the model and the experimental data, visible in Fig. 9a-c, is excellent when acoustic coupling was neglected (L_a=0), but the electrical component of the coupling (C_e) and a poor grounding L_p were considered. S_{21} in Fig. 9a-c is measured at three different values of detuning between the two elements. Note, that in this model, L_p is the only adjustable parameter, and its value was the same for all three values of the detuning. A more detailed explanation about the effects of the individual circuit elements on the crosstalk can be found in section S3 of the Supporting Information.

The authors wish to point out that, although the modeled parasitic effects are, in this case, negligible, and would not affect the characterization of the designed array, this does not invalidate the model itself. The model proposed faithfully represents those mentioned effects and allows its identification in a simple and sufficiently precise way. Therefore, it may be applicable in other cases where such effect could be not negligible.

Note, that while our discussion of the cross-talk is based on the results of the X-crystallographic direction only, all of the above arguments apply equally to the other crystallographic directions up to the substitution of the appropriate values for the geometric, elastic, and piezoelectric parameters.

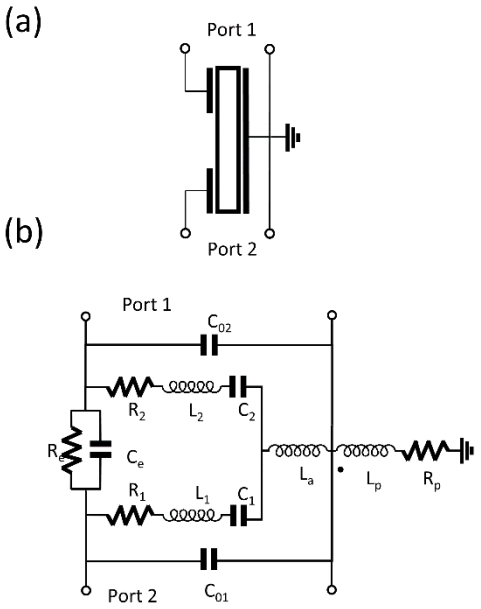

Fig. 10. Cross-talk analysis: the equivalent circuit model. Array element topology (a), and its equivalent circuit representation (b), used to analyze crosstalk between the adjacent array elements. The topology corresponds to two resonators sharing a common electrode that is grounded. R_1, L_1, C_1 and R_2, L_2, C_2 comprise the motional branches of the BvD circuits used to represent each of the two quartz resonators (array elements). C_{01} and C_{02} account for the static capacitances between the electrodes of each of the two resonators. Coupling between the resonators is modeled with a combination of a capacitor C_e, inductor L_a, and a resistor R_e; the latter accounts for the losses. Parasitic elements L_p and R_p model the ground path. Further details can be found in the text.

D. Behavior of the Arrays in Liquid

As a final step, we checked whether the arrays functioned in liquids. These results are merely illustrative; details of the microfluidic cell and the detailed validation of array performance in fluids will be presented in a future publication.

The change in the resonance frequency and bandwidth upon transfer from air to water is expected to satisfy the Kanazawa-Gordon-Mason (KGM) relation [8], [57], [58], $\Delta f + i\Delta\Gamma = -\frac{(1-i)\sqrt{2f_{res}^3\rho_{liq}\eta_{liq}}}{Z_q\sqrt{2\pi}}$, where Z_q is the acoustic impedance of AT quartz (8.84×10^6 kg m^{-2} s^{-1}), f_{res} is the fundamental resonance frequency of the array element, ρ_{liq} is the density of the liquid, and η_{liq} its viscosity. The results are shown in Table III, where the theoretically expected values and experimentally obtained values for the arrays and various individual resonators are shown.

TABLE III
AIR-TO-WATER FREQUENCY AND BANDWIDTH

Condition	Δf kHz	ΔΓ kHz	Accuracy	
			rms (Δf) kHz	rms (ΔΓ) kHz
150 MHz (n = 1)				
Theory	-113 ± 0.6	113 ± 0.6		
Experiment (arrays)	-103 ± 16	116 ± 12	19 (16%)	13 (11%)
35 MHz (f_0 = 5 MHz, n = 7)				
Theory	-1.78	1.78		
Experiment	-1.83 ± 0.05	1.67 ± 0.009	0.05 (3%)	0.12 (7%)
150 MHz (f_0 = 50 MHz, n = 3)				
Theory	-37	37		
Experiment	-40 ± 2	38 ± 2	3 (8%)	2 (5%)
100 MHz (n = 1)				
Theory	-60	60		
Experiment	-62 ± 2	53.0 ±0.5	2.4 (4%)	7.3 (12%)

Data shifts for the arrays prepared in this study compared with those for the individual sensors. Theoretical values were calculated using the KGM relationship. For the arrays, the resonance frequencies, f_{res}, of the individual elements (Fig. 5) were used in the calculations. Errors are standard deviations, accuracy values are rms deviations between the measured and the theoretical values. Water density and viscosity at 22ºC were used in the calculations.

The values presented in Table III show that the air-to-water shifts can be measured with these arrays with the accuracy comparable to that observed with the individual HFF resonators. We also note that the frequency shift due to the change from air to water, ~

– 113 kHz, is much smaller than the separation between the fundamental and the first inharmonic modes, which is ~ 300 kHz (see section III.C.2).

IV. Conclusion

The main result of this work is the 24-element monolithic, high fundamental frequency (HFF) QCMD array design and the physical and electrical characterization of the arrays manufactured according to this design. Special emphasis in characterizing the arrays was placed on surface roughness, inharmonic sidebands, and analysis of the interactions between the elements of the array, as these aspects will detrimentally affect array performance and may limit its biosensing functionality.

Reproducibility of array manufacturing has been demonstrated. The roughness of the working surface of the array was ~ 1 nm, that is to say, comparable with that of other commercially available QCMD resonators. Resonance frequencies of the array elements of 149 MHz ± 0.2 MHz and quality factors of $(1.2 \pm 0.1)\times10^4$, averaged over 26 different arrays, have been obtained. Inharmonic modes do not disturb operation with liquids, since a separation between the fundamental and the first observed inharmonic of ~ 300 kHz was achieved. This value significantly exceeds the change in frequency and bandwidth due to the immersion of the arrays in aqueous media. The behavior of the array elements fits very well with that of the individual resonators of the same design and predictions of the FEM simulations. Finally, we demonstrate that the performance of the arrays in liquid is comparable to that of the individual HFF resonators.

A significant part of our work deals with the interactions between the array elements. We show that there are no detectable acoustic interactions between the array elements for our array geometry. This conclusion is consistent with the theoretical predictions and is supported by the results of the geometry-specific FEM simulations. We also observed differences between the experimental S_{21} shape and FEM simulations results. Using an equivalent circuit model based on the MCF topology, we show that these differences are explained entirely by parasitic impedances from the grounding of the resonators. This model can be useful for the general design of monolithic HFF QCMD arrays; since it provides a simple tool that allows a fast simulation of the interferences between array elements and a mean to identify the causes and try to avoid them.

We expect our arrays to be useful for biosensing applications and our results to investigators wishing to design their own high-performance monolithic HFF QCMD arrays.

ACKNOWLEDGMENT

The authors would also like to thank Jorge Martínez from the Laboratory of High Frequency Circuits (LCAF) of the Universitat Politècnica de València (UPV) for assistance with profilometry, and Manuel Planes, José Luis Moya, Mercedes Tabernero, Alicia Nuez and Joaquin Fayos from the Electron Microscopy Services of the UPV for helping with the AFM, and SEM measurements. M. Calero is the recipient of the doctoral fellowship BES-2017-080246 from the Spanish Ministry of Economy, Industry and Competitiveness (Madrid, Spain).

FUNDING SOURCES

This research was funded by Spanish Ministry of Economy and Competitiveness with FEDER funds (AGL 2016-77702-R) and European Commission Horizon 2020 Programme (Grant Agreement number H2020-FETOPEN-2016-2017/737212-CATCH-U-DNA - Capturing non-Amplified Tumor Circulating DNA with Ultrasound Hydrodynamics) for which the authors are grateful.

REFERENCES

[1] M. U. Ahmed, I. Saaem, P. C. Wu, and A. S. Brown, "Personalized diagnostics and biosensors: a review of the biology and technology needed for personalized medicine," *Crit. Rev. Biotechnol.*, vol. 34, no. 2, pp. 180–196, 2014.

[2] V. Gubala, L. F. Harris, A. J. Ricco, M. X. Tan, and D. E. Williams, "Point of Care Diagnostics: Status and Future," *Anal. Chem.*, vol. 84, no. 2, pp. 487–515, 2012.

[3] J. L. C. M. Dorne, J. L. C. M. Dorne, L. R. Bordajandi, B. Amzal, P. Ferrari, and P. Verger, "Combining analytical techniques, exposure assessment and biological effects for risk assessment of chemicals in food," *TrAC Trends Anal. Chem.*, vol. 28, no. 6, pp. 695–707, Jun. 2009.

[4] N. L. Anderson and N. G. Anderson, "The Human Plasma Proteome," *Mol. Cell. Proteomics*, vol. 1, no. 11, pp. 845–867, Nov. 2002.

[5] J. Kirsch, C. Siltanen, Q. Zhou, A. Revzin, and A. Simonian, "Biosensor technology: recent advances in threat agent detection and medicine," *Chem. Soc. Rev.*, vol. 42, no. 22, p. 8733, 2013.

[6] P. Arora, A. Sindhu, N. Dilbaghi, and A. Chaudhury, "Biosensors as innovative tools for the detection of food borne pathogens," *Biosens. Bioelectron.*, vol. 28, no. 1, pp. 1–12, 2011.

[7] P. . Patel, "(Bio)sensors for measurement of analytes implicated in food safety: a review," *TrAC Trends Anal. Chem.*, vol. 21, no. 2, pp. 96–115, Feb. 2002.

[8] D. Johannsmann, *The Quartz Crystal Microbalance in Soft Matter Research*. Cham: Springer International Publishing, 2015.

[9] Y. Montagut, J. Garcia, Y. Jimenez, C. March, A. Montoya, and A. Arnau, "QCM Technology in Biosensors," in *Biosensors - Emerging Materials and Applications*, InTech, 2011.

[10] M. D. Ward and D. A. Buttry, "In Situ Interfacial Mass Detection with Piezoelectric Transducers," *Science (80-.).*, vol. 249, no. 4972, pp. 1000–1007, Aug. 1990.

[11] I. Reviakine, D. Johannsmann, and R. P. Richter, "Hearing What You Cannot See and Visualizing What You Hear: Interpreting Quartz Crystal Microbalance Data from Solvated Interfaces," *Anal. Chem.*, vol. 83, no. 23, pp. 8838–8848, Dec. 2011.

[12] G. Sauerbrey, "Use of vibrating quartz for thin film weighing and microweighing," *Z. Phys.*, vol. 155, pp. 206–222, 1959.

[13] A. Grammoustianou and E. Gizeli, "Acoustic Wave–Based Immunoassays," in *Handbook of Immunoassay Technologies*, J. H. T. L. Sandeep K. Vashist, Ed. Elsevier, 2018, pp. 203–239.

[14] G. Papadakis, P. Palladino, D. Chronaki, A. Tsortos, and E. Gizeli, "Sample-to-answer acoustic detection of DNA in complex samples," *Chem. Commun.*, vol. 53, no. 57, pp. 8058–8061, 2017.

[15] C. March-Iborra, "High-Frequency phase shift measurement greatly enhances the sensitivity of QCM immunosensors," *Biosens. Bioelectron.*, vol. 65, pp. 1–8, 2015.

[16] L. Cervera-Chiner *et al.*, “High Fundamental Frequency Quartz Crystal Microbalance (HFF-QCM) immunosensor for pesticide detection in honey,” *Food Control*, vol. 92, pp. 1–6, Oct. 2018.

[17] Gunter K. Guttwein, Arthur D. Ballato, and Theodore J. Lukaszek, “VHF-UHF Piezoelectric Resonators,” 3,694,677, 1972.

[18] B. Zimmermann, R. Lucklum, P. Hauptmann, J. Rabe, and S. Büttgenbach, “Electrical characterisation of high-frequency thickness-shear-mode resonators by impedance analysis,” *Sensors Actuators B Chem.*, vol. 76, no. 1–3, pp. 47–57, Jun. 2001.

[19] J. Rabe, S. Büttgenbach, B. Zimmermann, and P. Hauptmann, “Design, manufacturing, and characterization of high-frequency thickness-shear mode resonators,” *Proc. Annu. IEEE Int. Freq. Control Symp.*, pp. 106–112, 2000.

[20] L. Rodriguez-Pardo, J. Fariña, C. Gabrielli, H. Perrot, and R. Brendel, “Resolution in quartz crystal oscillator circuits for high sensitivity microbalance sensors in damping media,” *Sensors Actuators B Chem.*, vol. 103, no. 1–2, pp. 318–324, Sep. 2004.

[21] R. Fernández, P. García, M. García, J. García, Y. Jiménez, and A. Arnau, “Design and Validation of a 150 MHz HFFQCM Sensor for Bio-Sensing Applications,” *Sensors*, vol. 17, no. 9, p. 2057, Sep. 2017.

[22] Virgil E. Bottom, *Introduction to quartz crystal unit design*. New York: Van Nostrand Reinhold, 1982.

[23] C. Kreutz *et al.*, “High frequency quartz micro balances: A promising path to enhanced sensitivity of gravimetric sensors,” *Sensors*, vol. 6, no. 4, pp. 335–340, 2006.

[24] J. Rabe, S. Büttgenbach, J. Schröder, and P. Hauptmann, “Monolithic miniaturized quartz microbalance array and its application to chemical sensor systems for liquids,” *IEEE Sens. J.*, vol. 3, no. 4, pp. 361–368, 2003.

[25] P. Kao, S. Doerner, T. Schneider, D. Allara, P. Hauptmann, and S. Tadigadapa, “A micromachined quartz resonator array for biosensing applications,” *J. Microelectromechanical Syst.*, vol. 18, no. 3, pp. 522–530, 2009.

[26] A. Tuantranont, A. Wisitsora-at, P. Sritongkham, and K. Jaruwongrungsee, “A review of monolithic multichannel quartz crystal microbalance: A review,” *Anal. Chim. Acta*, vol. 687, no. 2, pp. 114–128, 2011.

[27] P. Kao, D. Allara, and S. Tadigadapa, “Fabrication and performance characteristics of high-frequency micromachined bulk acoustic wave quartz resonator arrays,” *Meas. Sci. Technol.*, vol. 20, no. 12, p. 124007, Dec. 2009.

[28] D. Croux *et al.*, “Development of multichannel quartz crystal microbalances for MIP-based biosensing,” *Phys. Status Solidi Appl. Mater. Sci.*, vol. 209, no. 5, pp. 892–899, 2012.

[29] T. Tatsuma, Y. Watanabe, N. Oyama, K. Kitakizaki, and M. Haba, “Multichannel quartz crystal microbalance,” *Anal. Chem.*, vol. 71, no. 17, pp. 3632–3636, 1999.

[30] K. Jaruwongrungsee, U. Waiwijit, A. Wisitsoraat, M. Sangworasil, C. Pintavirooj,

and A. Tuantranont, “Real-time multianalyte biosensors based on interference-free multichannel monolithic quartz crystal microbalance,” *Biosens. Bioelectron.*, vol. 67, pp. 576–581, 2015.

[31] W. Tao, P. Lin, Y. Ai, H. Wang, S. Ke, and X. Zeng, “Multichannel quartz crystal microbalance array: Fabrication, evaluation, application in biomarker detection,” *Anal. Biochem.*, vol. 494, pp. 85–92, Feb. 2016.

[32] M. Nirschl *et al.*, “CMOS-integrated film bulk acoustic resonators for label-free biosensing,” *Sensors*, vol. 10, no. 5, pp. 4180–4193, 2010.

[33] J. Petri, S. Hochstädt, T. Nentwig, A. Pausch, A. Langhoff, and D. Johannsmann, “A Fast Electrochemical Quartz Crystal Microbalance,which Acquires Frequency and Bandwidth on Multiple Overtones,” *Electroanalysis*, vol. 29, no. 3, pp. 806–813, Mar. 2017.

[34] R. A. Sykes and W. D. Beaver, “High Frequency Monolithlc Crystal Filters with Posslble Application to Single Frequency and Single Side Band Use,” in *20th Annual Symposium on Frequency Control*, 1966, pp. 288–308.

[35] A. A. Vives, J. M. F. y D. L. Osorio, T. S. Devesa, and Y. J. Jiménez, *SISTEMAS ELECTRÓNICOS DE COMUNICACIONES I*. Valencia: Universitat Politècnica de València, 2000.

[36] S. Berg and D. Johannsmann, “Laterally coupled quartz resonators,” *Anal. Chem.*, vol. 73, no. 6, pp. 1140–1145, 2001.

[37] W. D. Beaver, “Analysis of Elastically Coupled Piezoelectric Resonators,” *J. Acoust. Soc. Am.*, vol. 43, no. 5, pp. 972–981, 1968.

[38] F. Lu, H. P. Lee, P. Lu, and S. P. Lim, “Finite element analysis of interference for the laterally coupled quartz crystal microbalances,” *Sensors Actuators, A Phys.*, vol. 119, no. 1, pp. 90–99, 2005.

[39] H. Iwata, “Multistage chemical etching for high-precision frequency adjustment in ultrahigh-frequency fundamental quartz resonators,” *IEEE Trans. Ultrason. Ferroelectr. Freq. Control*, vol. 52, no. 9, pp. 1435–1442, 2005.

[40] J. Liang, J. Huang, T. Zhang, J. Zhang, X. Li, and T. Ueda, “An experimental study on fabricating an inverted mesa-type quartz crystal resonator using a cheap wet etching process,” *Sensors (Switzerland)*, vol. 13, no. 9, pp. 12140–12148, 2013.

[41] Y. Nagaura, K. Kinoshita, and S. Yokomizo, “High-frequency, plano-convex quartz oscillators made by a dual-face lapping machine,” in *Proceedings of the 2000 IEEE/EIA International Frequency Control Symposium and Exhibition (Cat. No.00CH37052)*, 2000, pp. 255–259.

[42] J. R. Vig, “Chemically Polished Quartz,” in *31st Annual Symposium on Frequency Control*, 1977, pp. 131–143.

[43] J. R. Hunt and R. C. Smythe, “Chemically Milled VHF and UHF AT-Cut Resonators,” in *39th Annual Symposium on Frequency Control*, 1985, pp. 292–300.

[44] S. Buettgenbach, J. Rabe, B. Zimmermann, and P. R. Hauptmann, “High-frequency thickness-shear mode resonators for sensor application in liquids,” in

Advanced Environmental and Chemical Sensing Technology, 2001, vol. 4205, no. February 2001, p. 207.

[45] W. P. Hanson, "Chemically polished high frequency resonators," *Proc. 37th AFCS*, pp. 261–234, 1983.

[46] J. A. Rubio Lara, F. Bergler, S. J. Attwood, J. M. Edwardson, and M. E. Welland, "Ultra-flat Gold QCM Electrodes Fabricated with Pressure Forming Template Stripping for Protein Studies at the Nanoscale," *Langmuir*, 2019.

[47] R. P. Richter and A. Brisson, "QCM-D on mica for parallel QCM-D - AFM studies," *Langmuir*, vol. 20, no. 11, pp. 4609–4613, 2004.

[48] T. Abe, V. Hung, and M. Esashi, "Inverted mesa-type quartz crystal resonators fabricated by deep-reactive ion etching," *IEEE Trans. Ultrason. Ferroelectr. Freq. Control*, vol. 53, no. 7, pp. 1234–1236, Jul. 2006.

[49] V. N. Hung, T. Abe, P. N. Minh, and M. Esashi, "Miniaturized, highly sensitive single-chip multichannel quartz-crystal microbalance," *Appl. Phys. Lett.*, vol. 81, no. 26, pp. 5069–5071, 2002.

[50] J. Zhang, J. Liang, and T. Ueda, "Design and evaluation of a dual channel high frequency Quartz crystal Microbalance," *Proc. Int. Conf. Sens. Technol. ICST*, 2016.

[51] T. Abe and M. Esashi, "One-chip multichannel quartz crystal microbalance (QCM) fabricated by Deep RIE," *Sensors Actuators A Phys.*, vol. 82, no. 1, pp. 139–143, 2000.

[52] J. R. Vig, R. J. Brandmayr, and R. L. Filler, "Etching Studies on Singly and Doubly Rotated Quartz Plates," in *33rd Annual Symposium on Frequency Control*, 1979, pp. 351–358.

[53] L. Li, T. Abe, and M. Esashi, "Microfabricated smerical bi-convex quartz crystal microbalance array," *18th IEEE Int. Conf. Micro Electro Mech. Syst. 2005. MEMS 2005.*, pp. 327–330, 2005.

[54] W. Shockley, D. R. Curran, and D. J. Koneval, "Trapped-Energy Modes in Quartz Filter Crystals," *J. Acoust. Soc. Am.*, vol. 41, no. 4B, pp. 981–993, 1967.

[55] H. Jiang, "Finite element analysis on electrode structure of QCM," *2009 Chinese Control Decis. Conf. CCDC 2009*, pp. 3618–3621, 2009.

[56] E. Zampetti, S. Pantalei, A. Macagnano, E. Proietti, C. Di Natale, and A. D'Amico, "Use of a multiplexed oscillator in a miniaturized electronic nose based on a multichannel quartz crystal microbalance," *Sensors Actuators, B Chem.*, vol. 131, no. 1, pp. 159–166, 2008.

[57] K. K. Kanazawa and J. G. Gordon, "Frequency of a quartz microbalance in contact with liquid," *Anal. Chem.*, vol. 57, no. 8, pp. 1770–1771, 1985.

[58] W. P. Mason, *Piezoelectric crystals and their application to ultrasonics.* New York: Van Nostrand, 1950.

Román Fernández is a Research and Development manager at AWSensors and an Associated Professor at Universitat Politècnica de València (UPV), Spain. He received his Ph.D. degree from UPV in 2003. His current research interests are focused on acoustic wave sensors for biosensing applications.

María Calero obtained her bachelor and master's degree from Universitat Politècnica de València in 2015 and 2017 respectively in telecommunication engineering. She is currently developing her PhD about acoustic array sensors in Universitat Politècnica de València .

Dr. Ilya Reviakine is a chief application scientist at AWSensors and an Affiliate Professor at the University of Washington in Seattle. He specializes in biological surfaces and interfaces, interactions between biological systems (lipids, blood) and surfaces of artificial materials, and surface acoustic sensing. Previously, he led independent research groups in Spain and in Germany. As a recipient of the prestigious Alexander von Humboldt research fellowship, he worked on hydrodynamic effects in surface-acoustic sensing. His doctoral work on atomic force microscopy of biological macromolecules and their assemblies earned him a Paper of the Year award from the Journal of Structural Biology.

Dr. José Vicente García-Narbón, chief technology officer (CTO) at AWSensors, received the Telecommunications Engineering (2007) and Ph.D. degrees (2016) from Universitat Politècnica de València (UPV), Spain. Since 2002, he has been working on the design of electronics interfaces for piezoelectric sensors, precision electronics, embedded systems, and acoustic wave sensors and its applications.

María Isabel Rocha-Gaso received the B.S degree in Computer Engineering from the Universidad Nacional Autónoma de México (2006). In 2013, the Universitat Politècnica de València, and the Université catholique de Louvain, granted her the PhD degree in Electronic Engineering. Afterwards, she completed a CNRS one-year postoctoral position at the University of Lorraine, fully dedicated to a French-Canadian ANR research project. From 2015 to 2017, she was a Research Professor at the Universidad de Quintana Roo, Mexico, and currently, she is working at the company AWSensors, Spain. Her fields of expertise include: MEMS, biosensors, microfrabrication processes and piezoelectric acoustic wave sensors and applications.

Antonio Arnau received the Engineering and Ph.D. degrees from Universitat Politècnica de València (UPV), Spain, in 1990 and 1999, respectively. Since 1990 he has been working on the design of electronics and communication electronics circuits and acoustic wave sensors. His current research interests include piezoelectric transducers and applications. He is author of more than 50 international papers and books; he has 5 patents and has taught classes and seminars in over 25 foreign institutions. He has created two spin-off companies: AWSensors focused on acoustic sensors and its applications to biotechnology and AWSensors Diagnostics, focused on Point of Care, Point of Diagnostics and Mobile Health Applications market.

Yolanda Jimenez received the degree of Telecommunications Engineer and the PhD from Universitat Politècnica de València in 1999 and 2004, respectively. She had obtained more than 30 research publications and is co-author of 2 patents, both internationally extended and in operation by the Spin-off company UPV AWSensors, of which she is a founding partner. Since she joined to the staff of UPV in 2000, her research has been focused on acoustic wave sensors, particularly in piezoelectric resonators, including their modelling, applications with biosensors, design of characterization systems and development of mathematical algorithms for the extraction of the physical parameters of the sensor